INSTITUTE OF PHYSICS PUBLISHING SUPERCONDUCTOR SCIENCE AND TECHNOLOGY
Supercond. Sci. Technol. **15** (2002) 395–404 PII: S0953-2048(02)27901-4

Vortex pinning by natural defects in thin films of $YBa_2Cu_3O_{7-\delta}$

J M Huijbregtse[1], F C Klaassen[1], A Szepielow[1], J H Rector[1], B Dam[1], R Griessen[1], B J Kooi[2] and J Th M de Hosson[2]

[1] Faculty of Sciences, Division of Physics and Astronomy, De Boelelaan 1081, 1081 HV, Amsterdam, The Netherlands
[2] Department of Applied Physics, Materials Science Centre, University of Groningen, Nijenborgh 4, NL-9747 AG Groningen, The Netherlands

E-mail: dam@nat.vu.nl

Received 15 August 2001
Published 6 February 2002
Online at stacks.iop.org/SUST/15/395

Abstract

Although vortex pinning in laser-ablated $YBa_2Cu_3O_{7-\delta}$ films on (100) $SrTiO_3$ is dominated by threading dislocations (Dam B *et al* (1999) *Nature* **399** 439), many other natural pinning sites are present. To identify the contribution from twin planes, surface corrugations and point defects, we manipulate the relative densities of *all* defects by post-annealing films with various as-grown dislocation densities, n_{disl}. While a universal magnetic field B dependence of the transport current density $j_s(B, T)$ is observed (independently of n_{disl}, temperature T and the annealing treatment), the defect structure changes considerably. Correlating the microstructure to $j_s(B, T)$, it becomes clear that surface roughness, twins and point defects are not important at low magnetic fields compared to linear defect pinning. Transmission electron microscopy indicates that threading dislocations are not part of grain boundaries nor are they related to the twin domain structure. We conclude that $j_s(B, T)$ is essentially determined by pinning along threading dislocations, naturally induced during the growth process. Even in high magnetic fields, where the vortex density outnumbers n_{disl}, it appears that linear defects stabilize the vortex lattice by means of the vortex–vortex interaction.

1. Introduction

The early observation of both high-transport current densities (typically between 10^{11} and 10^{12} A m^{-2} at low temperatures in zero magnetic field) and numerous structural defects in thin epitaxial films of the high-T_c superconductor $YBa_2Cu_3O_{7-\delta}$ motivated the identification of the strongest pinning defect [1]. Grain boundaries [2, 3], twin boundaries [4, 5], anti-phase boundaries [6–8], screw dislocations [9–12], edge dislocations [13, 14], precipitates [15–17] and surface roughness [18–21] have been suggested as good candidates. However, quantitative studies unambiguously relating the density of a *specific* defect to the transport current density characteristics were not performed, since the necessary control over the relative defect densities could not be achieved.

Only recently we reached a high degree of tunability for *threading dislocations* in thin films of $YBa_2Cu_3O_{7-\delta}$ by carefully manipulating the growth conditions [22]. This allowed us to relate the high transport current densities in films to strong pinning of vortices along dislocations in a semi-quantitative way [23]: a plateau B^* was found in the magnetic field dependence of the transport current density $j_s(B)$, which is directly proportional to the measured density of *all* dislocations (i.e., both edge, screw and dislocations of mixed character). The proportionality constant was determined to be $0.7\Phi_0$ at low temperatures, where $\Phi_0 = 2.068 \times 10^{-15}$ Tm^2 is the flux quantum, showing that dislocations are the main origin of the high currents. Subsequently, Klaassen *et al* [24] revealed the existence of a similar plateau in the dynamical relaxation rate below B^*. Moreover, the temperature dependence of both B^* and $j_s(B < B^*)$ was explained in terms of the Bose glass theory [25, 26], taking thermal fluctuations and the actual shape of the vortex-pin potential into account.

In the present paper, we focus our attention to alternative natural pinning sites (twin boundaries, precipitates, point defects and surface roughness) that are operative in combination with threading dislocations. In order to manipulate the relative densities of *all* defects, we perform annealing experiments on films with different as-grown dislocation densities. Indeed significant changes are found, both in the transport current characteristics and in the microstructure of these films. As a result, the contribution from the alternative pinning sites compared to linear defect pinning can be identified.

2. Experimental procedures

C-axis oriented, 110 nm thick $YBa_2Cu_3O_{7-\delta}$ films are deposited by means of pulsed laser deposition (PLD). An optical beam homogenizer ensures a spatially homogeneous laser spot on the target, which is essential for a reproducible deposition process [27]. The laser energy density J is set at 1.4 J cm^{-2}, as measured at the target. The $YBa_2Cu_3O_{7-\delta}$ films are deposited from a rotating polycrystalline, high density, tetragonal $YBa_2Cu_3O_{6+x}$ target (PRAXAIR >99.999% pure raw materials) on low miscut SrO-terminated (100) $SrTiO_3$ substrates [28], measuring $10 \times 10 \times 1.0$ mm^3. The target–substrate distance d_{T-S}, substrate temperature T_{sub} and oxygen pressure p_{O_2} are varied from 3.5 to 3.0 cm, 750 to 850 °C (as measured with a pyrometer) and 15 to 35 Pa, respectively, in order to decrease the dislocation density. The threading dislocation density of these films is determined by counting the number of square, sharp-bottomed etch pits formed upon applying a dislocation sensitive wet-chemical etchand (1 vol% Br in ethanol) [22].

Using these setting, we prepare a series of films with threading dislocation densities of 28, 50 and 68 μm^{-2} (see section 3). These films are divided into two parts; one part of each film is subjected to a two-step post-anneal [29]. First, these parts are quickly heated (15 °C min^{-1}) in a quartz tube oven to the annealing temperature $T_a = 800$ °C in a flowing Ar + 3% O_2 mixture (flow of 1.01 min^{-1}) and kept at this temperature for $t_a = 30$ min. Subsequently the samples are cooled down (2.0 °C min^{-1}) to 500 °C, changing to a 100% O_2 atmosphere around 600 °C. The films are kept in this second annealing stage for another 30 min and then slowly cooled down (<2 °C min^{-1}). In the first stage, during heating the $YBa_2Cu_3O_{7-\delta}$ films go through the orthorhombic-to-tetragonal structural phase transition (losing oxygen) in the low oxygen content atmosphere, further arrangement takes place at T_a and when cooling the films go through the tetragonal-to-orthorhombic transition (taking up oxygen) in the 100% oxygen atmosphere. The second annealing stage is incorporated to ensure full oxygenation.

As-deposited and post-annealed parts of the *same* film are compared in superconducting and microstructural properties as a function of the as-grown threading dislocation density. First, the transport current density $j_s(B, T)$ is measured on a ring geometry by means of capacitive torque magnetometry [24, 30] for temperatures $4.2 \leqslant T \leqslant 80$ K, applying magnetic-fields $B \leqslant 7$ T at an angle of 10° from the *c*-axis. The dimensions of the ring are a diameter of 3.0 mm and a width of 125 μm. The high magnetic-field regime is probed by sweeping the magnetic field at a rate of 40 mT s^{-1} (from 0 to 7 T). To determine the characteristic field accurately, additional low field sweeps (up to 1 T) are performed at a sweep rate of 1 mT s^{-1}. Microstructurally, the *c*-axis lattice parameter and mosaicity $\Delta\omega_{005}$ are determined by x-ray diffraction (XRD) with a RIGAKU rotating anode diffractometer (Cu Kα radiation), performing $\theta-2\theta$ scans from the 001 up to the 008-reflection and ω scans around the 005-reflection, respectively. The film thickness t was determined from the frequency of the Laue oscillations around the 001-reflection [31]. Rutherford backscattering spectrometry (RBS) angular scans are performed around the [001] direction to study the crystallinity, using 2.0 MeV He^+. To analyse the surface morphology of as-grown, post-annealed and wet-etched films, we use atomic force microscopy (AFM) in the tapping mode (NANOSCOPE IIIa multimode system). Finally, the resistivity ρ is recorded as a function of temperature T ($80 < T < 300$ K), using a four-probe configuration in combination with a well-defined strip geometry (0.50×4.0 mm^2).

A second series of samples was prepared under identical conditions as the first series in order to check if (part of) the effects reported here are due to small differences in the preparation procedure. As the microstructural parameters of both series are identical, we can exclude this possibility. Moreover, the microstructure of some additional films (deposited under comparable deposition conditions) is studied by transmission electron microscopy (TEM), both in cross section and in planar-view. Low magnification and high resolution TEM measurements are performed in a JEOL 4000 EX/II microscope operating at 400 kV (point resolution of 0.165 nm). Cross section specimens are prepared by a standard procedure: face-to-face glued specimens in cross-section geometry are polished down to a final thickness of about 15 μm using a Tripod polisher, followed by a 4 kV ion milling. To prevent damaging the $YBa_2Cu_3O_{7-\delta}$ film it turned out to be essential to use liquid-nitrogen cooling during this ion milling. Plan-view specimens were ground, dimpled and ion milled from one side in order to obtain an electron transparent area just in the film surface. Care was taken to prevent contamination of the surface during TEM specimen treatment.

3. Effect of post-annealing

3.1. Transport current

We measured the transport current density $j_s(B, T)$ in films with as-grown dislocation densities n_{disl} of 28 μm^{-2} (low) and 68 μm^{-2} (high) before and after the post-annealing procedure, see figure 1. The current density exhibits the behaviour well-known for linear defect pinning [23]: it is constant up to the characteristic field B^* (as indicated by arrows) and decays rapidly above this field. Both B^* and $j_s(B < B^*)$ strongly depend on temperature. Comparing the as-grown and post-annealed parts of the low n_{disl} sample, it is clear that there is no significant difference. Typically, $B^*(T = 4.2\,\text{K}) = 30$ mT and $j_s(B = 0, T = 4.2\ \text{K}) = 6 \times 10^{11}$ A m^{-2}. On the other hand, in the high n_{disl} sample we distinguish two significant effects: (i) B^* reduces by annealing and (ii) $j_s(B < B^*)$ increases. For instance, B^* goes down from 120 to 90 mT at

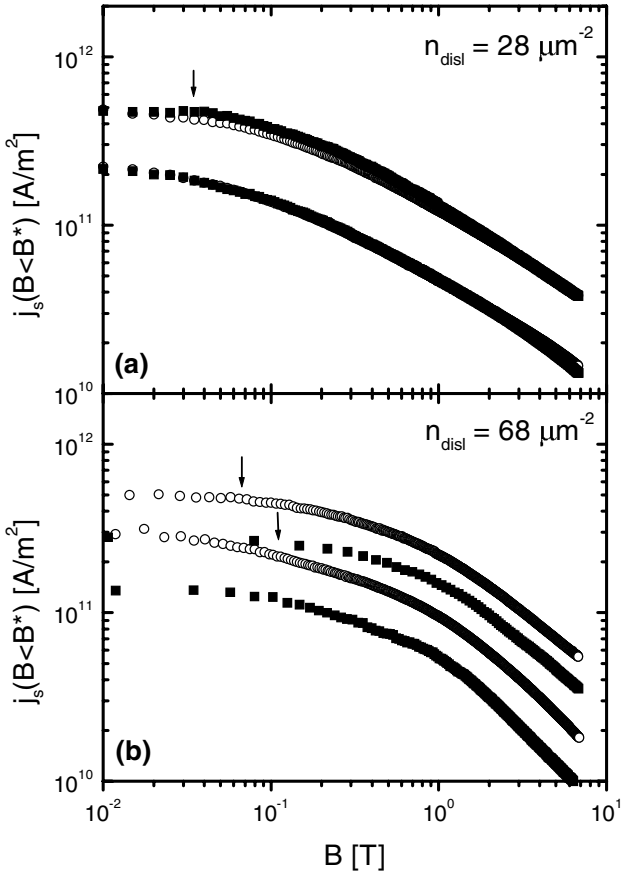

Figure 1. Influence of post-annealing on the magnetic field dependence of the transport current density $j_s(B)$ in 110 nm thick $YBa_2Cu_3O_{7-\delta}$ films deposited on (100) $SrTiO_3$ with different *as-grown* dislocation densities (n_{disl}): (*a*) a low $n_{disl} = 28\ \mu m^{-2}$ sample and (*b*) a high $n_{disl} = 68\ \mu m^{-2}$ sample at temperatures $T = 10$ and 40 K for the as-deposited (solid squares) and post-annealed (open circles) parts of the *same* sample. The arrows indicate the characteristic field B^* at 10 K.

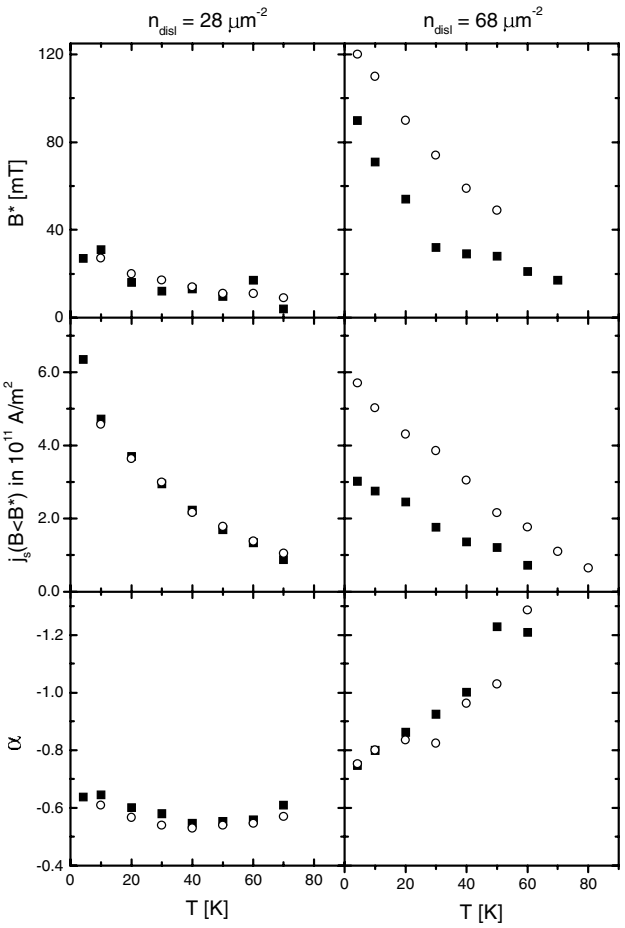

Figure 2. Comparing the influence of post-annealing on the transport current density $j_s(B, T)$ in 110 nm thick $YBa_2Cu_3O_{7-\delta}$ films on (100) $SrTiO_3$ with a low ($n_{disl} = 28\ \mu m^{-2}$, left column) and high ($n_{disl} = 68\ \mu m^{-2}$, right column) as-grown dislocation density. Shown are the temperature dependence of: (top panel) the characteristic field $B^*(T)$, (middle panel) the low magnetic field transport current density $j_s(B < B^*, T)$, and (lower panel) the high magnetic field power-law exponent $\alpha(T)$ for the as-deposited (solid squares) and post-annealed parts (open circles).

4.2 K, while $j_s(B = 0, T = 4.2\ \text{K})$ increases from 3×10^{11} to 6×10^{11} A m^{-2}.

We can capture the essence of the magnetic field dependence of $j_s(T)$ in three phenomenological parameters (see figure 2). While the low field behaviour is determined by both $B^*(T)$ and $j_s(B < B^*, T)$, the high field behaviour can be approximated by a power-law dependence, $j_s(B \gg B^*, T) \propto B^{\alpha(T)}$. Comparing the low and high n_{disl} sample, it appears that $j_s(B < B^*, T)$ is independent of the dislocation density after the annealing procedure. However, the high field behaviour is very different: films with a high as-grown dislocation density show a much quicker drop in j_s than films with a low dislocation density. We find α ($4.2 < T < 70$ K) ≈ -0.65 for the low n_{disl} sample, while $\alpha(T)$ decreases from -0.75 to -1.3 with T for the high n_{disl} sample, in agreement with previous findings [24]. It is important to note that $\alpha(T)$ is independent of the post-annealing treatment.

To correlate these characteristics in the superconducting current density to pinning by various natural defects, we now investigate the microstructure of the films before and after the post-annealing procedure in detail.

3.2. Microstructure

The annealing procedure takes place at a temperature comparable to the average deposition temperature (typically, $T_{sub} \approx T_a = 800\ ^\circ$C) of the laser-ablated $YBa_2Cu_3O_{7-\delta}$ films. Therefore, we expect clear changes in the microstructure.

(i) *Surface roughness*. In figure 3, AFM height images of three films deposited at decreasing substrate temperature $T_{sub} = 850$, 800 and 750 °C (increasing dislocation density) are shown before and after the post-annealing treatment. The as-grown surface morphology consists of semi-regularly spaced islands separated by trenches. Within the trenches some deeper depressions can be distinguished, corresponding to the sites where threading dislocations emerge [22]. Since dislocations are situated *around* the islands in as-deposited films, the island density n_{island} and dislocation density are proportional (the proportionality constant being close to 1) [22]. Therefore, n_{island} can be used as a quick measure for n_{disl}. Upon annealing the island density decreases, suggesting

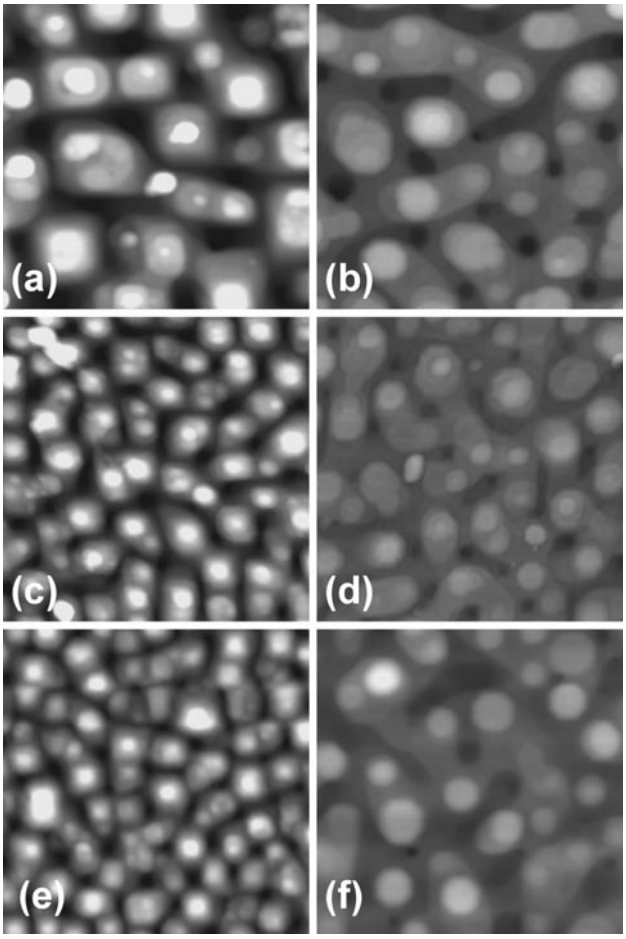

Figure 3. Effect of post-annealing on the surface morphology. AFM height images ($1.0 \times 1.0\ \mu m^2$) of 110 nm thick $YBa_2Cu_3O_{7-\delta}$ films on (100) $SrTiO_3$ with different as-grown dislocation densities n_{disl} after deposition (left column) and after the post-annealing procedure (right column): (*a, b*) $n_{disl} = 28\ \mu m^{-2}$, (*c, d*) $n_{disl} = 50\ \mu m^{-2}$ and (*e,f*) $n_{disl} = 68\ \mu m^{-2}$. Each pair of images is taken on as-grown and post-annealed parts of the *same* film. Upon post-annealing both the island density and the surface roughness decrease. The effects are more pronounced for higher n_{disl}. The height scale is 50 nm (bright is high, dark is low); the image conditions (colour table, contrast, etc.) are the same for all images.

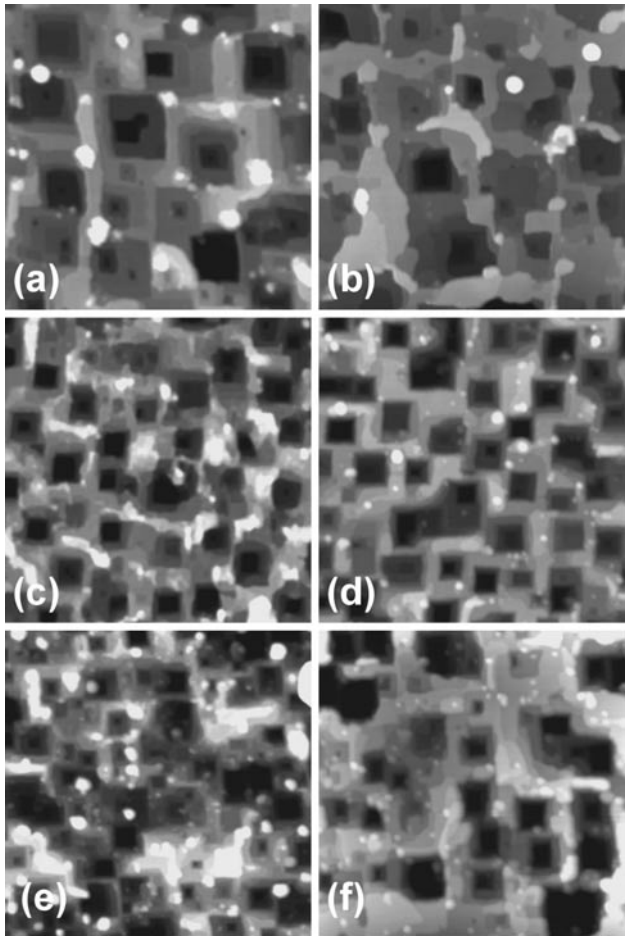

Figure 4. Effect of post-annealing on the dislocation density (n_{disl}), as determined by counting the number of etch pits formed upon dislocation specific wet-chemical etching. Shown are AFM height images ($1.0 \times 1.0\ \mu m^2$) of the same films as in figure 3 after Br-ethanol etching the as-grown (AD, left column) and post-annealed (PA, right column) parts: (*a*) AD: $n_{disl} = 28\ \mu m^{-2}$ and (*b*) PA: $n_{disl} = 24\ \mu m^{-2}$, (*c*) AD: $n_{disl} = 50\ \mu m^{-2}$ and (*d*) PA: $n_{disl} = 51\ \mu m^{-2}$, (*e*) AD: $n_{disl} = 68\ \mu m^{-2}$ and (*f*) PA: $n_{disl} = 43\ \mu m^{-2}$. Post-annealing only affects n_{disl} in films with a high as-grown dislocation density. The height scale is 50 nm.

that the dislocation density has changed. In addition, the surface flattens considerably (note that the same height scales are used). For example, the root-mean-square (rms) roughness decreases from 4 to 2 nm, typically.

(ii) *Dislocation density*. To check if the dislocation density changes upon annealing, we perform wet-chemical etching experiments. In figure 4, AFM images corresponding to the same films as in figure 3 are shown after etching in 1% Br-ethanol, to reveal all threading dislocations. Here, n_{disl} is determined by averaging the results obtained for different areas of the same film, using etch times between 20 and 90 s. We find that the dislocation density decreases significantly only in films with the *highest* as-grown dislocation density (from $n_{disl} = 68\ \mu m^{-2}$ to $43\ \mu m^{-2}$). Indeed dislocation annihilation is expected to be easier in these films, since the average distance d_{disl} between dislocations is relatively small ($d_{disl} \approx 1/\sqrt{n_{disl}}$). It is important to note that the correlation between the island density and dislocation density is lost upon post-annealing: the dislocation density outnumbers the island density.

(iii) *Crystallinity*. A measure often used for the crystallinity of $YBa_2Cu_3O_{7-\delta}$ films is the full width at half maximum of its 005 rocking curve, $\Delta\omega_{005}$. In figure 5(*a*) an example of such an XRD measurement is shown (ω scan). Upon annealing $\Delta\omega_{005}$ reduces from 0.16° to 0.14°, showing that the lateral (in-plane) correlation length has increased. This is a general trend: $\Delta\omega_{005}$ decreases upon post-annealing, the effect being larger for higher n_{disl}. However, films with a high as-grown dislocation density (deposited at a low substrate temperature) always have slightly broader rocking curves, even after the post-annealing procedure ($\Delta\omega_{005} \approx 0.2^\circ$). Finally, we performed RBS [001] channel measurements on the film with the highest as-grown dislocation density, comparing the as-deposited and post-annealed part, see figure 5(*b*). Upon annealing, the channel minimum yield for the Ba

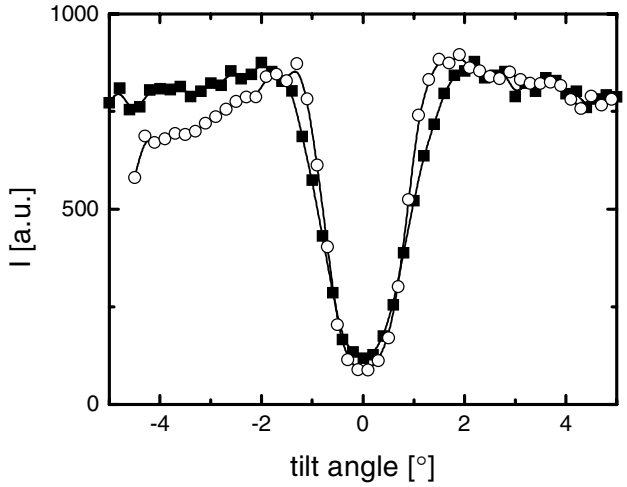

Figure 5. Effect of post-annealing on the crystallinity of 110 nm thick $YBa_2Cu_3O_{7-\delta}$ films on (100) $SrTiO_3$: (*a*) XRD 005 rocking curve (ω scan) for the film with an as-grown dislocation density $n_{disl} \approx 50\ \mu m^{-2}$, and (*b*) RBS [001] channel dip measurement for the Ba signal of the film with an as-grown $n_{disl} = 68\ \mu m^{-2}$. Since both the XRD peak and the RBS channel dip become more narrow, we conclude that the crystallinity improves somewhat upon annealing.

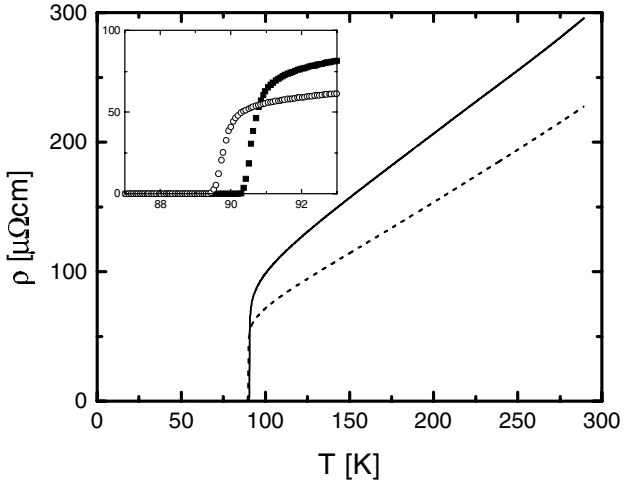

Figure 6. Effect of post-annealing on a 110 nm thick $YBa_2Cu_3O_{7-\delta}$ film on (100) $SrTiO_3$ with as-grown dislocation density $n_{disl} = 68\ \mu m^{-2}$: The resistivity ρ as a function of temperature T, revealing that both ρ and T_c go down.

signal χ_{Ba} decreases from 3.7% to 2.5%, while the full width at half minimum of the [001] channel dip decreases (from 1.9° to 1.6°), confirming the improved crystallinity. The RBS results also indicate that as-deposited high n_{disl} films are already of a good crystallinity [32].

(iv) *Doping*. The films go through the tetragonal ($YBa_2Cu_3O_{6+x}$) to orthorhombic ($YBa_2Cu_3O_{7-\delta}$ structural phase transition twice during the post-annealing process. Therefore, the oxygen content of the films may have changed considerably. As both the *c*-axis lattice constant and the resistivity ρ of the film are sensitive functions of the oxygen content, we performed XRD and electrical transport measurements on the as-grown and post-annealed parts.

We find that the 007 peak in the θ–2θ scan shows a shift to higher angles (smaller *c*-axis) and a clearer $K_{\alpha 1}$–$K_{\alpha 2}$ splitting (indicative of the improved crystallinity). The increase in intensity also shows evidence of improved crystallinity in the direction along the *c*-axis, although part of the increase may result from a slightly different alignment. Calculating the *c*-axis length from the 00*l*-reflections for $l = 1$–8, we observe a general trend: on average, the *c*-axis decreases from 11.70 to 11.69 Å upon annealing, independent of the dislocation density. This effect can be attributed to (i) an increase in oxygen content, (ii) an improvement of the crystallinity, including Y/Ba disorder and O chain ordering or a combination of both. To separate these effects, let us examine the resistive transition more closely. By post-annealing *both* the resistivity ρ and the T_c go down for all films, see figure 6 for an example. The decrease in ρ is larger in films with a higher as-grown n_{disl}. An improvement of crystallinity alone would lower ρ and increase T_c, whereas an increase in charge carrier density above the optimal doping lowers both ρ and T_c. Therefore, we conclude that the crystallinity improves and the films are slightly overdoped after annealing.

Summarizing, the effects of post-annealing on the microstructure are more pronounced in films with a higher as-grown dislocation density.

4. Vortex pinning mechanisms

In the first approximation, vortex pinning originates from the condensation energy that a vortex gains by passing through regions where the superconducting order parameter is depressed (defects). In the case of a high density of randomly distributed point defects, the vortex minimizes its total energy by taking advantage of these defects. However, this process is limited by the increase in elastic energy due to vortex bending and its increase in length. By applying a current in the *ab*-plane, the vortex (parallel to the *c*-axis) experiences a Lorentz force and it starts to move above some threshold current density. In this weak collective pinning picture a relatively small current density is needed to depin a vortex, which does not depend on the applied magnetic field. Clearly, this picture fails to explain our $j_s(B, T)$ measurements, pointing to vortices being pinned by defects correlated over a significant length (strong pinning). Ignoring vortex–vortex interactions, with increasing magnetic field vortices will initially be strongly pinned by such correlated defects until the vortex density outnumbers the defect density. The additional vortices are only weakly pinned and the current density that can be passed without dissipation decreases.

In our $YBa_2Cu_3O_{7-\delta}$ thin films different types of correlated disorders are naturally present, among which are linear defects (dislocations), planar defects (twin boundaries), precipitates and thickness fluctuations. The microstructural effects of post-annealing described above allow for an investigation of the influence of different natural defects on vortex pinning in these films as probed by the transport current density $j_s(B, T)$.

4.1. Pinning by linear defects

We find that the characteristic *shape* of $j_s(B, T)$ is independent of both the dislocation density and the post-annealing procedure. In agreement with a previous study [23, 24], the characteristic field at low temperatures is determined by the *total* dislocation density as measured by wet-chemical etching, according to:

$$B^* \approx 0.7 n_{disl} \Phi_0. \quad (1)$$

Both B^* and $j_s(B < B^*)$ are functions of the superconducting parameters [i.e., the coherence length $\xi = \xi(T)$ and the magnetic penetration depth $\lambda = \lambda(T)$]. The temperature dependence of these parameters in combination with thermal fluctuations are responsible for the observed decrease in $B^*(T)$ and $j_s(B < B^*, T)$ with temperature [24].

Post-annealing the sample with a high as-grown n_{disl} (see figure 2) reduces B^*. This is a direct consequence of the annihilation of dislocations during annealing ($n_{disl} = 68 \rightarrow 43\ \mu\text{m}^{-2}$, see figure 4). Indeed, the characteristic field corresponds well with the measured density of dislocations after post-annealing, following equation (1). However, the reason for the increase in $j_s(B < B^*)$ is not *a priori* clear. In the single vortex regime, where vortex–vortex interactions can be neglected, the current density is determined by the depinning of a vortex from a linear defect. Therefore, the same value of $j_s(B < B^*)$ is expected for all films, independently of n_{disl}. Before post-annealing, however, films with a low as-grown dislocation density usually carry somewhat larger currents than films with a high as-grown n_{disl}, see figures 1 and 2 for an example. This is a consequence of the *method* used to increase n_{disl}. Since high dislocation densities are induced at relatively low substrate temperatures (750 °C in this investigation), the corresponding rocking curves are usually broader (typically, $\Delta\omega_{005} \approx 0.2^\circ$) and the resistivities are higher ($\rho_{RT} \approx 300\,\mu\Omega\,\text{cm}$) compared to low n_{disl} films ($\Delta\omega_{005} \approx 0.1^\circ$ and $\rho_{RT} \approx 250\,\mu\Omega\,\text{cm}$). These effects are indicative of a poorer crystallinity and lower doping. Post-annealing (partly) corrects for both issues and the current increases in the high n_{disl} film. The improvement in overall crystallinity (including oxygen stoichiometry) of the films ensures that the depression in the superconducting order parameter as well as ξ and λ are the same for all films. Due to the sharpening of the pinning potential upon annealing, $j_s(B < B^*)$ approaches a universal value of 6×10^{11} A m^{-2} at 4.2 K, characteristic for the pinning of a single vortex by a dislocation. Surprisingly, the overdoping upon annealing does not affect the current density.

Given the dominant role of linear defects as pinning centres in these films, we started a cross-sectional TEM investigation for threading dislocations. Generally, dislocations are difficult to observe in a cross section [33], as their density is relatively low and their core size is small [34]. Despite difficulties in the TEM sample preparation, we were able to identify threading dislocations in a sample with a high dislocation density, see the '2-beam' bright field images in figure 7 (strong diffracting beam parallel to the *c*-axis). Here, an example of a dislocation originating at the substrate–film interface and extending up to the surface in a direction close to the *c*-axis is shown. By varying the *g*-vector in dark field, the threading dislocations cannot be discerned when *g* is parallel to the *c*-axis, suggesting that these are *screw* dislocations. This specific

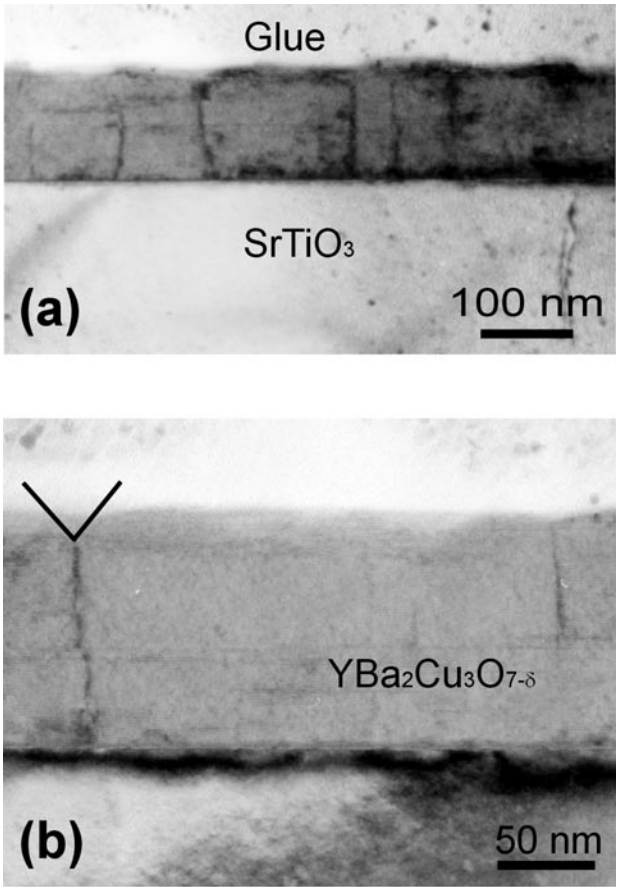

Figure 7. Low magnification cross-sectional '2-beam' bright field TEM images of a 120 nm $YBa_2Cu_3O_{7-\delta}$ films on (100) $SrTiO_3$ with a high dislocation density (this specific film was shortly etched in Br/ethanol): (*a*) a high density of threading dislocations originating at the interface and extending all the way up to the surface can be distinguished and (*b*) the correlation between a threading dislocation and an etch pit is schematically shown; simultaneous observation of etch pits and dislocations turned out to be difficult (only by varying the defocus a correlation could be established).

film was shortly etched in 1% Br/ethanol in order to correlate etch pits and dislocations directly. By varying the defocus either etch pits or dislocations can be discerned. Therefore, simultaneous observation of both etch pits and threading dislocations is difficult. However, it appears that etch pits are present at the positions where dislocation lines emerge at the surface, as schematically indicated in figure 7(*b*). We note that preferential etch pit formation was recently unambiguously related to threading dislocations of screw *and* mixed character in films of GaN on (0001)-sapphire [35], combining AFM and cross-sectional TEM analysis.

4.2. Pinning by planar defects

A network of planar defects provides for an alternative source of strong pinning [36]. As shown by Doornbos *et al* [37], in a network of planar defects, spaced by a distance *d*, vortex–vortex interactions are expected to become important when the vortex spacing is of the order of λ. This gives rise to a characteristic field of the order

$$B^* \approx \frac{2\Phi_0}{\lambda d}. \quad (2)$$

Below, we consider three types of planar defects: twin boundaries, anti-phase boundaries and (low-angle) grain boundaries. Also, the relation between threading dislocations, twinning dislocations and low-angle grain boundaries is investigated.

4.2.1. Twin boundaries During the tetragonal-to-orthorhombic phase transition upon cooling down, (110) and ($\bar{1}$10) twins form. In figure 8, a planar view TEM image is shown of an as-grown sample with a very low dislocation density (about 10 μm^{-2} as estimated from the island density), showing that twins of each orientation are distributed in domains. Since the twin planes are parallel to the *c*-axis, these planar defects might give rise to matching field behaviour. In our experiment, the annealing must have changed the twin structure, since the films are cooled down in a very different way: the as-deposited sample is quenched in pure oxygen (>100 mbar) to room temperature within a few minutes, whereas the post-annealed sample is cooled down much more slowly. It has been shown that the post-annealed samples exhibit longer and more ordered twins due to the improved kinetics [38]. Yet, no significant difference in $j_s(B, T)$ is found in the low n_{disl} film (see figure 1), indicating that twin boundaries are relatively unimportant compared to linear defect pinning.

The twin boundaries are distributed in domains, containing either (110) or ($\bar{1}$10) twin boundaries. To relieve the mismatch between the domains, twinning dislocations [39] with a dislocation line parallel to the *c*-axis will be formed at the domain boundaries if the mutual distance between subsequent twin planes in the domains is large enough (i.e., larger than 50 nm). However, this distance of the film investigated is generally less than 40 nm (see figure 8(*b*)), which avoids the necessity of introducing twinning dislocation at the domain boundaries. Furthermore, assuming that the threading dislocations are twinning dislocations, they are expected to be distributed in a network which is characterized by a length scale of about 1 μm, see figure 8. Clearly, this length scale is much larger than the threading dislocation spacing [22]. Apparently, the deformations are elastically accommodated and we conclude that twinning dislocations are not present in our $YBa_2Cu_3O_{7-\delta}$ films.

4.2.2. Anti-phase boundaries Anti-phase boundaries may be induced by the vicinal steps in the substrate (0.4 nm in height, corresponding to $\approx c/3$) [40]. Indeed an anisotropy in j_s was reported in these miscut samples: along the vicinal steps a higher current density is found than perpendicular to them. We used substrates with a vicinal angle of only 0.15° [28] and the number of anti-phase boundaries is expected to be small. Although we previously found indications for the existence of a network of anti-phase boundaries [41], in our present TEM investigations we did not detect such anti-phase boundary networks. We attribute this difference to (i) the use of better quality substrates (smaller miscut angles, different supplier, better characterization) and (ii) our new substrate preparation and cleaning procedure, yielding essentially SrO-terminated (100) $SrTiO_3$ substrates [28]. We find that, in contrast to TiO_2-terminated substrates, the pattern of vicinal steps on SrO-terminated substrates cannot be traced back by AFM in $YBa_2Cu_3O_{7-\delta}$ films thicker than one monolayer [28]. Although anti-phase boundaries are absent in our films on SrO-terminated substrates, we find current densities that are as high as those obtained on miscut samples [6–8]. In our opinion, vortex pinning in films on miscut substrates may still be dominated by threading dislocations. The observed anisotropy could as well arise from an anisotropy in crystallinity. As shown here, crystallinity influences the magnitude of the transport current and can, therefore, account for an anisotropy in j_s.

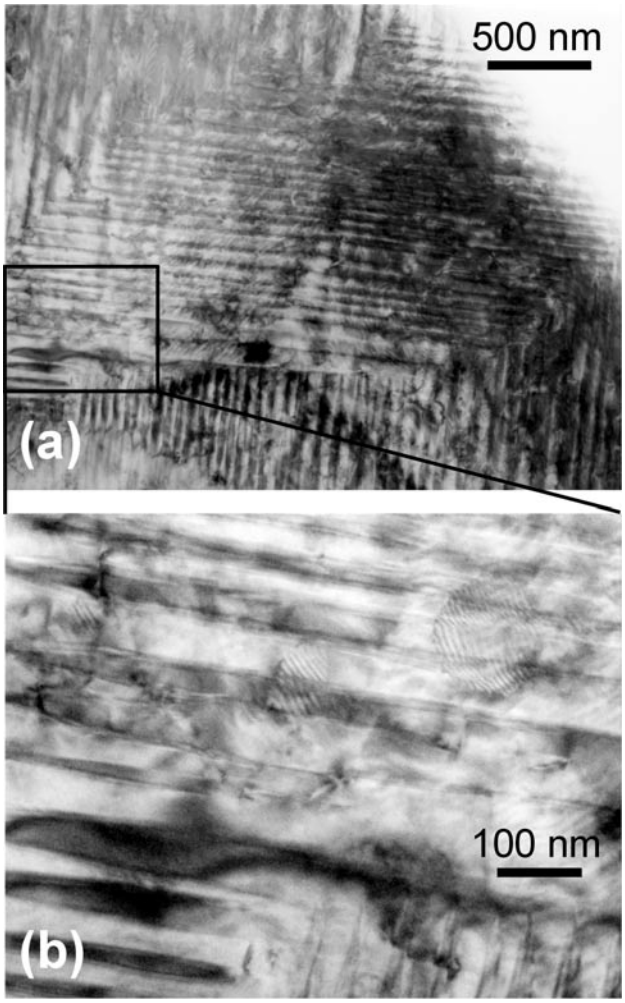

Figure 8. Planar view TEM images of a 500 nm $YBa_2Cu_3O_{7-\delta}$ films on (100) $SrTiO_3$ with a very low dislocation density ($n_{disl} \approx 10$ μm^{-2}), showing (*a*) domains containing only one orientation of twin planes and (*b*) a close-up of such a domain, showing that the mutual distance between subsequent twin planes within the domain is generally less than 40 nm. Note that the length scale of the twin domains is much larger than the average distance between threading dislocations (250 nm).

4.2.3. (Low-angle) grain boundaries As discussed above, any network of planar defects might give rise to matching field behaviour, see equation (2). In particular, the observed island morphology of the films suggest that the islands could be separated by (hidden) grain boundaries [3]. Since large angle (>5°) grain boundaries strongly affect the magnitude of the transport current density [42], the observed large currents

imply that only *low-angle* (<5°) grain boundaries can be present. We previously found a scaling between the island density n_{island} and threading dislocation density n_{disl} and observed that the dislocations are situated around the islands [22]. Therefore, it is tempting to assume that the threading dislocations are distributed in low-angle grain boundaries, separating the growth islands. We can calculate the angle ϑ between adjacent islands using the Shockley–Read formula [43]:

$$d_{disl} = \frac{b}{2\sin(\vartheta/2)} \tag{3}$$

where b is the magnitude of the Burger's vector and d_{disl} is the average distance between dislocations ($d_{disl} \approx 1/\sqrt{n_{disl}}$). Although we find *screw* dislocations, we assume that $b = 0.39$ nm[3]. Taking the extremes for the dislocation density, we find $0.12 < \vartheta < 0.18°$. In our opinion, these misorientations are elastically accommodated and do not influence the coupling between islands.

In addition, upon annealing films with a high as-grown n_{disl}, the one-to-one correspondence between the island and dislocation density is lost, see figures 3 and 4. This allows us to discriminate between individual linear defects and dislocations located in low angle grain boundaries. For this particular high n_{disl} film, we find that upon annealing (i) n_{disl} decreases from 68 to 43 μm^{-2}, (ii) n_{island} decreases faster from 66 to 30 μm^{-2}, while (iii) $B^*(4.2\,\mathrm{K})$ drops from 120 mT to 90 mT. Following equation (1), $B^*(PA)/B^*(AD) = 0.75$ resembles $n_{disl}(PA)/n_{disl}(AD) = 0.63$ and not $n_{island}(PA)/n_{island}(AD) = 0.45$. Here, we used the notation AD = as-deposited and PA = post-annealed. This confirms that B^* is determined by the dislocation density rather than some other defect related to the island density (like low-angle grain boundaries)[4]

Finally, in our TEM investigation we were unable to reveal any grain boundaries, both in cross section and in planar view. We find that the atomic layers are continuous over tens of microns apart from some stacking faults parallel to the *ab*-plane (also introduced by the ion milling during TEM sample preparation) and we conclude that grain boundaries are absent.

4.3. Pinning by point defects and precipitates

At high fields, a weak effect of point disorder on $j_s(B, T)$ was demonstrated [44] in $YBa_2Cu_3O_{7-\delta}$ films after the introduction of point defects by low energetic (25 MeV) irradiation with ^{16}O ions. In our picture of linear defect pinning, above the characteristic field all linear defects pin one vortex and the additional vortices will be pinned by other defects [12]. Therefore, at fields $B \gg B^*$ point defects may play a role in combination with linear defects. Surprisingly, the characteristic power-law dependence at high fields does not change upon post-annealing, see figures 1 and 2. Yet, the relative amount of different types of point defects must have changed, implying that, in first approximation, point defects do not determine the high magnetic field behaviour.

In fact, the robustness of the high field behaviour suggests that even for $B \gg B^*$ linear defects still play an important role [24]. The high-field power-law exponent $\alpha(T)$ is either close to -0.5 (low n_{disl}) or -1 (high n_{disl}), which can be understood from vortex shear between unpinned vortices, and vortices pinned by linear defects [45] and collective pinning by linear defects [26], respectively. The cross-over takes place at a dislocation density of the order $1/\lambda^2 \approx 45$ μm^2 at low temperatures [24]. Although the details of the pinning mechanism operative at high fields are not clear to us at this moment, all results point to linear defects still being the effective pinning sites at $B \gg B^*$. Also a high density of precipitates facilitates vortex pinning [15–17], since a vortex can gain condensation energy. In the case of $YBa_2Cu_3O_{7-\delta}$ films mostly Y_2O_3 precipitates have been found [46]. By planar view TEM we indeed find some Y_2O_3 precipitates. Since their density is relatively low (4 μm^2 in the sample shown in figure 8), we infer that the pinning effect of these precipitates is insignificant.

4.4. Surface roughness effects

In our explanation for the higher current densities in films compared to single crystals so far, we left out the contribution from thickness fluctuations [18–21]. In principle, roughness contributes to the pinning of vortices, since a vortex may lower its energy by minimizing its length [19]. Obviously, roughness effects are more important in films compared to single crystals due to their relatively small thickness. As the substrate–film interface is atomically flat [47], we concentrate on the effect of surface roughness. Assuming a sinusoidal thickness modulation $\delta t \sin(2\pi x/L)$, the pinning force per unit length f_p is calculated to be [19]:

$$f_p \approx \frac{2\pi\varepsilon_0\delta t}{Lt}. \tag{4}$$

In this expression, ε_0 is the line energy of a vortex [48]. Clearly, smoother surface modulations reduce vortex pinning due to surface corrugations. We find that upon annealing the surface roughness is greatly reduced (the rms roughness after annealing is about half of the roughness of the as-grown samples). However, we find no corresponding decrease in the transport current density upon annealing. Therefore, we conclude that the contribution of the surface to $j_s(B, T)$ is negligible compared to linear defect pinning.

5. Conclusions

We correlated the microstructure of $YBa_2Cu_3O_{7-\delta}$ thin films, laser ablated on (100) $SrTiO_3$ substrates, to the superconducting current density $j_s(B, T)$. The defect structure of these films is characterized by threading dislocations, surface corrugations, twin planes, precipitates and point defects. As a tool to manipulate the relative amount of these defects, we employ an *ex-situ* post-annealing treatment at a temperature close to the average deposition temperature. We find that:

[3] As a low angle grain boundary consists of an array of edge dislocations we take b equal to the average in-plane lattice constant of $YBa_2Cu_3O_{7-\delta}$ (≈0.39 nm).

[4] This effect is even more clear in sputtered $YBa_2Cu_3O_{7-\delta}$ films, where the island density is orders of magnitude smaller than the measured threading dislocation density[22,23].

(i) Threading dislocations are the dominant pinning sites for vortices, giving rise to the well-known matching field behaviour in $j_s(B, T)$: it is constant up to a characteristic field $B^*(T)$ and decreases rapidly according to a power-law $B^{\alpha(T)}$ above B^*. On average, $j_s(B < B^*, T)$ decreases slightly with increasing as-grown dislocation density n_{disl}. We attribute this effect to the somewhat poorer film quality of these films, which determines the shape of the pinning potential. Annealing the films reveals a universal $j_s(B < B^*, 4.2\,\mathrm{K}) = 6 \times 10^{11}$ A m^2, as expected for linear defect pinning in the single vortex regime. As a result, the transport characteristics can now be summarized by three phenomenological parameters only: B^*, $j_s(B < B^*)$ and α. Here, B^* is proportional to n_{disl}, while α is close to -0.5 for $n_{disl} \lesssim 45\ \mu\mathrm{m}^{-2}$ and close to -1 for $n_{disl} \gtrsim 45\ \mu\mathrm{m}^{-2}$, indicative of a shear and a collective pinning mechanism, respectively.

(ii) It is shown that some dislocations are annihilated while annealing films with a high as-grown n_{disl} (small dislocation spacing), which is accompanied by a decrease in B^*. Moreover, the one-to-one correspondence between the island density n_{island} and n_{disl} is lost upon annealing. This allows us to discriminate between individual dislocations and dislocations being part of low-angle grain boundaries. As B^* follows the measured n_{disl} and not n_{island}, the islands are not loosely connected by means of low-angle grain boundaries (or some other defect related to the island size).

(iii) By post-annealing, the surface roughness and the point defect density decrease, while the twin structure also changes. Since both $j_s(B, T)$ and n_{disl} are not affected at all in films with a low as-grown n_{disl}, these type of defects do not contribute to vortex pinning at low magnetic fields compared to linear defect pinning. In addition, it is shown that overdoping does not affect the magnitude of $j_s(B, T)$.

As a final step, we performed cross-sectional and planar view transmission electron microscopy investigations to verify these conclusions. Indeed, threading dislocations are observed. It is shown that these dislocations are not part of low-angle grain boundaries nor are they related to the twin domain boundaries. In addition, the precipitate density was shown to be very low and anti-phase boundaries were not be detected.

We conclude that (at low temperature) threading dislocations fully determine the vortex pinning properties of thin films of $YBa_2Cu_3O_{7-\delta}$, reconfirming earlier findings [23]. Remarkably, even the high magnetic field behaviour is determined by the presence of linear defects. Apparently, the vortex–vortex interactions stabilize the vortex lattice up to fields as high as 7 T. We conclude that $YBa_2Cu_3O_{7-\delta}$ films contain a relatively low density of growth-induced, ordered threading dislocations that are extremely interesting both from a technological and a fundamental point of view.

Acknowledgments

Use of the RBS facility at the AMOLF-FOM institute in Amsterdam is gratefully acknowledged. This work is part of the research programme of FOM (stichting Fundamenteel Onderzoek der Materie), which is financially supported by NWO (stichting Nederlands Wetenschappelijk Onderzoek).

References

[1] Ramesh R, Hwang D M, Venkatesan T, Ravi T S, Nazar L, Inam A, Wu X D, Dutta B, Thomas G, Marshall A F and Geballe T H 1990 *Science* **247** 57
[2] Harshavardhan K S, Rajeswari M, Hwang D M, Chen C Y, Sands T, Venkatesan T, Tkaczyk J E, Lay K W and Safari A 1992 *Appl. Phys. Lett.* **60** 1902
[3] Mezzetti E, Gerbaldo R, Ghigo G, Gozzelino L, Minetti B, Camerlingo C, Monaco A, Cuttone G and Rovelli A 1999 *Phys. Rev.* B **60** 7623
[4] Safar H, Coulter J Y, Maley M P, Foltyn S, Arendt P, Wu X D and Willis J Q 1995 *Phys. Rev.* B **52** R9875
[5] Villard C, Koren G, Cohen D, Polturak E, Thrane B and Chateignier D 1996 *Phys. Rev. Lett.* **77** 3913
[6] Haage T, Zegenhagen J, Li J Q, Habermeier H-U, Cardona M, Jooss Ch, Warthmann R, Forkl A and Kronmüller H 1997 *Phys. Rev.* B **56** 8404
[7] Jooss Ch, Warthmann R, Kronmüller H, Haage T, Habermeier H-U and Zegenhagen J 1999 *Phys. Rev. Lett.* **82** 632
[8] Jooss Ch, Warthmann R and Kronmüller H 2000 *Phys. Rev.* B **61** 12433
[9] Gerber Ch, Anselmetti D, Bednorz J G, Mannhart J and Schlomm D G 1991 *Nature* **350** 279
[10] Hawley M, Raistrick I D, Beery J G and Houlton R J 1991 *Science* **251** 1587
[11] Mannhart J, Anselmetti D, Bednorz J G, Catana A, Gerber Ch, Müller K A and Schlomm D G 1992 *Z. Phys.* B **86** 177
[12] Douwes H, Kes P H, Gerber Ch and Mannhart J 1993 *Cryogenics* **33** 486
[13] Pan V M, Kasatkin A L, Svetchnikov V L and Zandbergen H W 1993 *Cryogenics* **33** 21
[14] Diáz A, Mechin L, Berghuis P and Evetts J E 1998 *Phys. Rev. Lett.* **80** 3855
[15] Murakami M, Morita M, Doi K and Miyamoto K 1989 *Japan. J. Appl. Phys.* **28** 1189
[16] Watanabe K, Matsushita T, Kobayashi N, Kawabe H, Aoyagi E, Hiraga K, Yamane H, Kurosawa H, Hirai T and Muto Y 1990 *Appl. Phys. Lett.* **56** 1490
[17] Tian Y J, Guo L P, Li L, Zhou Y Q, Yang Y, Zhao Z X, Xu S F, Lu H B, Zhou Y L, Chen Z H, Cui D F and Yang G Z 1994 *Appl. Phys. Lett.* **65** 234
[18] McElfresh M, Miller T G, Schaiffer D M, Reifenberger R, Muenchenhausen R E, Hawley M, Foltyn S R and Wu X D 1992 *J. Appl. Phys.* **71** 5099
[19] Kes P 1997 *Materials and Crystallographic Aspects of HT_c-Superconductivity* ed E Kaldis (Dordrecht: Kluwer) p 407
[20] Jooss Ch, Forkl A, Warthmann R, Habermeier H-U, Leibold B and Kronmüller H 1996 *Physica* C **266** 235
[21] Jooss Ch, Forkl A and Kronmüller H 1996 *Physica* C **268** 87
[22] Huijbregtse J M, Dam B, van der Geest R C F, Klaassen F C, Elberse R, Rector J H and Griessen R 2000 *Phys. Rev.* B **62** 1338
[23] Dam B, Huijbregtse J M, Klaassen F C, van der Geest R C F, Doornbos G, Rector J H, Testa A M, Freisem S, Martinez J C, Stäuble-Pümpin B and Griessen R 1999 *Nature* **399** 439
[24] Klaassen F C, Doornbos G, Huijbregtse J M, van der Geest R C F, Dam B and Griessen R 2001 *Phys. Rev.* B **64** 18 4523
[25] Nelson D R and Vinokur V M 1992 *Phys. Rev. Lett.* **68** 2398
[26] Nelson D R and Vinokur V M 1993 *Phys. Rev.* B **48** 13060
[27] Huijbregtse J M, Dam B, Rector J H and Griessen R 1999 *J. Appl. Phys.* **86** 6528

[28] Huijbregtse J M, Rector J H and Dam B 2001 *Physica* C **351** 183
[29] Feenstra R, Christen D K, Klabunde C E and Budai J D 1992 *Phys. Rev.* B **45** 7555
[30] Qvarford M, Heeck K, Lensink J G, Wijngaarden R J and Griessen R 1992 *Rev. Sci. Instrum.* **63** 5726
[31] Lin W-J, Hatton P D, Baudenbacher F and Santiso J 1998 *Appl. Phys. Lett.* **73** 2995
[32] Hüttner D, Meyer O, Reiner J and Linker G 1996 *Nucl. Instr. and Meth. in Phys. Res.* B **118** 578
[33] Schlomm D G, Anselmetti D, Bednorz J G, Broom R F, Catana A, Frey T, Gerber Ch, Günterhodt H-J, Lang H P and Mannhart J 1992 *Z Phys.* B **86** 163
[34] Gao Y, Merkle K L, Bai G, Chang H L M and Lam D J 1991 *Physica* C **174** 1
[35] Hino T, Tomiya S, Miyajima T, Yanashima K, Hashimoto S and Ikeda M 2000 *Appl. Phys. Lett.* **76** 3421
[36] Gurevich A and Cooley L D 1994 *Phys. Rev.* **50** 13563
[37] Doornbos G, Dam B, Martinez J C, Surdeanu R, Poppe U and Griessen R 1997 *Physica* C **282–287** 2303
[38] Lairson B M, Streiffer S K and Bravman J V 1990 *Phys. Rev.* B **42** 10067
[39] Zhu Y and Suenaga M 1992 *Phil. Mag.* A **66** 457
[40] Wen J G, Træholt C and Zandbergen H W 1993 *Physica* C **205** 354
[41] Dam B, Træholt C, Stäuble-Pümpin B, Rector J and De Groot D G 1997 *J. Alloys Compd.* **251** 27
[42] Heinig N F, Redwing R D, Nordman J E and Larbalestier D C 1999 *Phys. Rev.* B **60** 1409
[43] Hirth J P and Lothe J 1982 *Theory of Dislocations* (New York: Wiley)
[44] Roas B, Hensel B, Saemann-Ischenko G and Schultz L 1989 *Appl. Phys. Lett.* **54** 1051
[45] Wördenweber R 1992 *Phys. Rev.* B **46** 3076
[46] Catana A, Broom R F, Bednorz J G, Mannhart J and Schlom D G 1992 *Appl. Phys. Lett.* **60** 1016
[47] Wen J G, Morishita T, Koshizuka N, Traeholt C and Zandbergen H W 1995 *Appl. Phys. Lett.* **66** 1830
[48] Blatter G, Feigel'man M V, Geshkenbein V B, Larkin A I and Vinokur V M 1994 *Rev. Mod. Phys.* **66** 1125